Title

Effect of fluorination and Li-excess on the Li migration barrier in Mn-based cathode materials

Journal

Journal of Materials Chemistry A, 8(38)

ISSN

2050-7488

Authors

Jadidi, Zinab
Chen, Tina
Xiao, Penghao
et al.

Publication Date

2020-10-06

DOI

10.1039/d0ta06415g

Peer reviewed

Effect of fluorination and Li-excess on the Li migration barrier in Mn-based cathode materials

Zinab Jadidi[ab], Tina Chen[ab], Penghao Xiao[c], Alexander Urban[d], Gerbrand Ceder[ab*]

[a] Department of Materials Science and Engineering, UC Berkeley, Berkeley, CA 94720, USA

[b] Materials Sciences Division, LBNL, Berkeley, CA 94720, USA

[c] Materials Science Division, Lawrence Livermore National Laboratory, Livermore, CA 94550, USA

[d] Department of Chemical Engineering, Columbia University in the City of New York, NY 10027, USA

[*] Email: gceder@berkeley.edu

ABSTRACT

Disordered rocksalt (DRX) Li-rich transition metal (TM) oxides, especially those based on Mn, are prospective high-energy-density cathode materials for the next generation of Li-ion batteries that use earth abundant metals. Fluorine substitution on the oxygen sublattice has been shown to reduce oxygen redox by lowering the average anion valence and increasing the amount of redox-active TM, and simultaneously improve energy density, average voltage and capacity retention. While these benefits of fluorination are well established, it is not well understood how F affects Li transport and therefore the rate performance of Mn-based DRX cathodes. Herein, we investigate the effects of both F substitution and the accompanying Li-excess on Li migration barriers using first-principles calculations. We demonstrate that F has a small negative effect on Li migration barriers while Li-excess decreases Li migration barriers. Because fluorination enables more Li-excess, these results do not predict any detrimental impact on Li transport.

INTRODUCTION

Li-rich transition metal (TM) oxides are considered prospective high-energy-density cathode materials for the next generation of lithium ion batteries (LIBs) (1–5). An especially attractive class of Li-rich cathode materials are those based on Mn redox due to their large energy densities, widespread availability, cost efficiency, and relative stability of the Mn^{4+} valence state. In addition, these Mn-based cathodes (6,7) do not contain Co and Ni, which are limited resources (8). In Li-rich compositions the TM redox capacity is typically lower than the Li-content capacity. Accessing high capacities therefore requires significant oxygen redox participation (9,10), which commonly leads to more oxygen gas release and thus poor capacity retention (11–14). Substitution of some O by F lowers the average valence of the cations thereby increasing the TM redox capacity and reducing oxygen loss during cycling (15). While the impact of fluorination on the redox capacity is well understood, it is also crucial to understand how F substitution affects the Li transport. Previous work has shown that while small amounts of F reduce the percolation of Li migration paths, larger F contents (> 15%) improve percolation (16). In this work we investigate the effect F has on the local migration barrier in Mn based compounds.

We use orthorhombic-$LiMnO_2$ (o-$LiMnO_2$) as a prototypical material as it exhibits similar structural motifs to Mn-based Li-rich cathodes (namely Mn and Li in octahedral sites on the same anion FCC lattice), and it has a larger variety of anion environments compared to layered TM oxide cathodes. As such it is a good ordered model system to evaluate the effect of F on Li mobility.

Van der Ven et al (17) proposed that Li migration in rocksalt structures can occur through a single or divacancy mechanism. In general, the activation energy of the divacancy mechanism

is lower in layered cathodes making it the active mechanism as soon as any Li is removed from the structure (18,19).To fully understand the interplay between the effect of F and Li-excess, we calculate the migration barrier for both mechanisms for varying amounts of F substitution and Li-excess and for different anion occupancies around the migrating Li. Based on the results from our calculations, we conclude that F substitution has only a small effect on Li migration barriers while Li-excess has a strong favorable effect and decreases the Li migration barrier in agreement with previous publications (20). Hence, we do not expect any detrimental impact on Li ion transport when fluorination is used as a design strategy to increase the amount of TM redox and reduce oxygen loss from cathode materials.

$LiMnO_2$ has an orthorhombic *Pmmn* (o-$LiMnO_2$) structure (21) with close-packed oxygen lattice in which octahedrally coordinated Li and Mn align themselves in corrugated layers. All MnO_6 octahedra share a common edge with each other, and those with Mn^{3+} experience Jahn-Teller distortion due to the preference for the high spin state ($t_{2g}^3e_g^1$) (22). Half of the anion sites are coordinated by 2 Li and 4 Mn, and the other half are coordinated by 4 Li and 2 Mn. Because of the weaker binding between TM and F compared to that between TM and O, F tends to substitute for O sites with maximal Li coordination (23). When Li-excess is introduced into the composition, some anion sites become coordinated by 5 Li and 1 Mn. These anion sites are preferred substitution sites to introduce F as they generate only 1 TM-F bond (23).

Li can migrate either through the anion dumbbell between two octahedral sites, called an oxygen dumbbell hop (ODH) mechanism, as shown in Figure 1a (bottom), or through an intermediate tetrahedral site that shares anion-coordinated faces with the initial and final octahedra, called a tetrahedron site hop (TSH) mechanism, as shown in Figure 1b (bottom) (17). In general, the ODH mechanism only occurs during single vacancy migration due to repulsion by

the cations around the migration path. In the presence of at least one more Li vacancy, the TSH is energetically preferred in layered materials (17).

In the TSH mechanism, we categorize the hop type based on the number of TM that occupy octahedra that face-share with the intermediate tetrahedral site. For example, if there are 0 nearest-neighbor TM to the intermediate tetrahedron, we call this a 0-TM channel, consistent with notation in the literature (20). Because the intermediate tetrahedron has 4 nearest-neighbor octahedral sites, two of which are the initial and final sites of the Li hop, a relevant channel can only be categorized as 0-TM, 1-TM, or 2-TM.

METHODS

First-Principles Density Functional Theory calculations

We obtained structural energies from density functional theory (DFT) (24,25) using the generalized-gradient approximation (GGA) with the PBE exchange-correlation functional (26) and projector-augmented wave (PAW) method (27,28), as implemented in the Vienna ab-initio Package (VASP) package (29,30). We used a plane-wave cutoff of 520 eV in all of our calculations. In the voltage calculation, a Hubbard-U (31) correction was employed for Mn using the suggested U-value in the Materials Project (U= 3.9 eV) (32). For all the calculations, we used reciprocal space discretization of 25 K-points per $Å^{-1}$ and set the electronic convergence to 10^{-5} eV and the force convergence to -0.01 eV/Å. The nudged elastic band (NEB) method is used to compute diffusion activation barriers (33) based on five images along the diffusion paths for both single vacancy and divacancy migration mechanisms in both pristine o-$LiMnO_2$ and, 4%, 6% and 50% fluorinated o-$LiMnO_2$. All NEB calculations were performed using GGA without Hubbard-U correction in order to avoid potential convergence issues

associated with electron localization at various atomic centers along the migration path (34,35). Due to the directional dependence of the migration barriers, we also show the kinetically resolved activation barrier (KRA) (19).

Structural model

The pristine prototype structure o-$LiMnO_2$ (with space group pmmn) was obtained from the Materials Project and has materials ID mp-18767 (32). For the non-fluorinated structure and the highly fluorinated (50% F) structure, calculations were performed in a supercell of 64 atoms. Calculations of slightly fluorinated (4% F) structures were performed in a supercell with 96 atoms to isolate the effect of a single F on the diffusion barrier. The F is substituted on one of the anion sites that is coordinated to the maximal number of Li (coordination environment of 4 Li and 2 Mn). The extra Li that represents Li-excess generally strongly prefers to bond to F rather than to O. To account for this preference, the Li added to the structures substitutes for one of the two Mn bonded to the added F. After substituting the first O for F and an adjacent Mn for Li, we additionally substitute one more O, with the maximal Li local environment, for F to maintain charge neutrality (for the case of 4% F concentration). Note that the second F is substituted so that it is 4 atomic layers (~6 Å) away from the first F in order to isolate the effect of a single fluorine on the energy barrier. In the model structure with 50% fluorination, the same strategy is used as for the 4% fluorinated structure, except that the number of F and Li-excess substitution is higher. For the calculation of Figure 4 where there is no Li-excess in the structure, a background charge is introduced to maintain charge neutrality in order to isolate the effect of the location of F substitution. No charge background was introduced in other calculations.

RESULTS

A. Diffusion Mechanism in pristine o-$LiMnO_2$

A1: Single vacancy diffusion mechanism

All calculations are performed with the Nudged Elastic Band method (NEB) and Density Functional Theory in the GGA approximation. More details are provided in the Methods section. Because of the orthorhombic symmetry in o-$LiMnO_2$, the in-plane hop (path 1 in Figure 1a) and out-of-plane hop (path 2 in Figure 1a) are not the same. We find that the out-of-plane hop has a lower migration barrier (500 meV) than the in-plane hop (560 meV) due to the closer proximity of the migrating Li ion to Mn ions along the path. In the following discussion, we therefore generally consider the out-of-plane hop because of its lower barrier, and we use this out-of-plane barrier of 500 meV as a reference for other single vacancy hops. The minimum energy path (MEP) of the single vacancy hop is shown in Figure S1 of the supplementary information (SI).

Our result is consistent with the Li diffusion barrier previously calculated for the ODH path in monoclinic $LiMnO_2$ (500 meV) (36) in which the immediate local environment for Li diffusion via the single vacancy mechanism is similar.

A2: Divacancy diffusion mechanism

Figure 1b shows a divacancy diffusion mechanism proceeding through a 1-TM channel TSH. Migration proceeds through the face-sharing tetrahedral site which face-shares with one TM cation. Note that a given pair of octahedral sites is connected through two different TSH, one on each side of the oxygen dumbbell edge that is shared between the initial and final octahedron. For clarity we adopt the convention that in our figures the TSH path discussed is always depicted above the oxygen dumbbell. The activation energy of the divacancy hop in this scenario, as

calculated with NEB, is 240 meV, much smaller than the barrier for the out-of-plane single vacancy hop (500 meV). We also use this divacancy barrier in the non-fluorinated o-$LiMnO_2$ as a reference to compare with those in the presence of F and Li-excess.

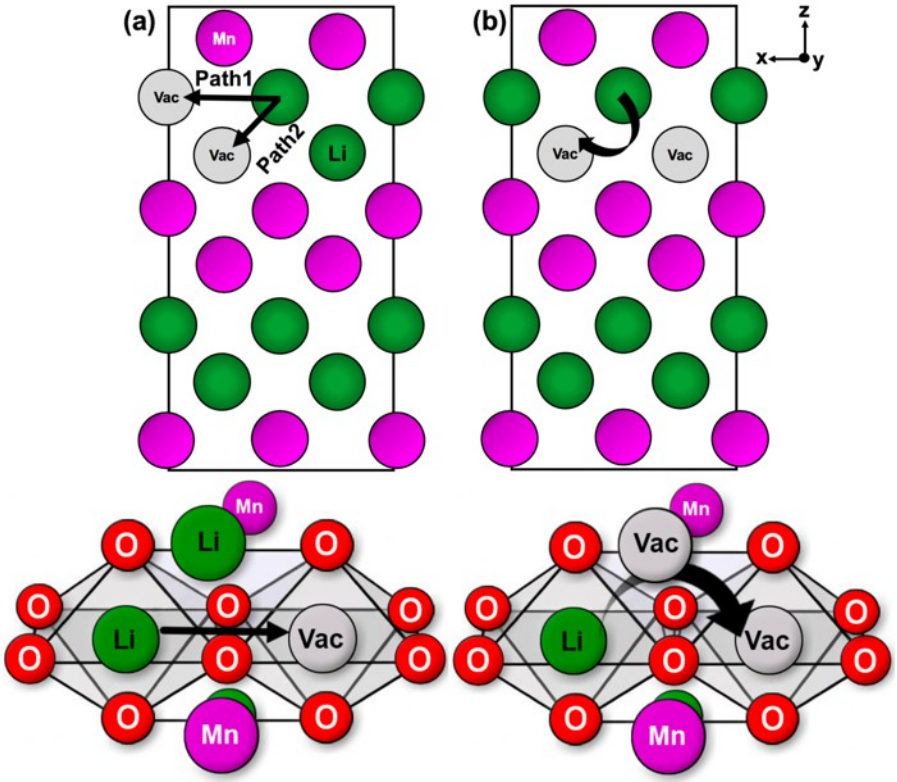

Figure 1: Possible Li migration paths in o-$LiMnO_2$ through the (a) single vacancy mechanism and (b) divacancy mechanism shown in the 010 plane (top) and in three-dimensional representations of the nearest neighbor cations along the path (bottom). Li hops occur along the trajectory shown by the black arrows. The single vacancy mechanisms can proceed via an in-plane hop (path 1) or an out-of-plane hop (path 2), whereas the divacancy mechanism is shown proceeding through an intermediate 1-TM channel. Note that the divacancy mechanism can only proceed through out-of-plane hops. Li, Mn, and O are shown as green, purple, and red spheres. O atoms are not shown in the top figures for clarity.

B. Single vacancy diffusion mechanism in presence of F and Li-excess

In F-substituted Li-excess compounds, Li sites with different local environments exist, so that the initial and final states, and thus the forward and backward migration barriers, of a Li hop may differ in energy, unlike the barriers in a symmetric local environment. In such a context, the kinetically-resolved activation (KRA) barrier is usually defined as the average between the forward and backward barrier (19). Figure 2 shows a summary of the diffusion barriers for single vacancy Li migration in different local environments. The horizontal bars show the magnitude of the forward (yellow striped bars), backward (solid blue bars), and KRA (dotted gray bars) barriers for each specific atomic configuration labeled on the *y* axis of the chart. The green vertically striped bar is the energy barrier in the pristine non-fluorinated $LiMnO_2$ structure. The local atomic configurations and trajectories of the migrating Li atoms are visualized adjacent to their respective bars and listed in the table. It should be noted that, while these figures capture the most local part of the environment around the migration path, the site occupancy outside of these pictures can also influence the energy. Three different trajectories are specified: (i) straight black arrow corresponding to ODH mechanism, (ii) bent black arrow corresponding to TSH mechanism, and (iii) slightly curved blue arrow in which the migrating Li does not fully go through the tetrahedral site. All the arrows show the direction of the forward barrier.

The asymmetry around the dumbbell in hops *a-c* causes the migration path for Li to bend toward the 0-TM tetrahedral channel rather than go straight through the dumbbell (ODH path) (Figure 1a). Such 0-TM channels are more likely to be found when Li-excess is present, which is facilitated by the incorporation of fluorine. The kinetically-resolved barriers are similar (270

meV, 310 meV, and 340 meV) independent of the amount of F or its position in the local environment, though the KRA's are clearly somewhat higher when F is present in the dumbbell.

Cases *d-f* are a family of 1-TM channel hops which are more likely to be found when there is no Li-excess nearby. Configuration *d* is the reference single vacancy ODH in o-$LiMnO_2$, which has a barrier of ~500 meV (Figure 1a). When 1 O atom coordinating the final site of the migration is replaced with F (environment *e*), the forward barrier remains approximately the same as in the pristine structure (490 meV), consistent with the fact that the initial state environment and the anion dumbbell occupation has not changed. The backward barrier in this environment is lower as the vacancy environment prefers F rather than O as one of its neighbors. However, when the F atom is substituted for one of the O atoms in the anion dumbbell (environment *f*), the KRA increases to ~640 meV, demonstrating the barrier's dependence on the location of the F along the path.

In both cases where 1 F has been added (environment *e* and *f*), the path bends slightly to avoid the anion dumbbell, which results in a path lying in between the ODH and the TSH pathways. This type of trajectory is shown with slightly curved blue arrows to distinguish them from the ODH and TSH mechanisms.

Several additional influences on the migration barrier can be extracted from the data in Figure 2. Comparing configurations *d* vs. *a* and *f* vs. *b* shows that the presence of Li-excess greatly decreases the barrier by more than 200 meV, which is in line with previous results showing that 1-TM channels are 200-300 meV higher in energy barrier than 0-TM channels (20).

By comparing *d* vs. *f* and *a* vs. *b*, it is apparent that the effect of F itself on the energy barrier is negative (i.e. results in higher migration barriers) but that the decrease in barrier from

nearby Li-excess outweighs the increase in barrier from F, resulting in an overall decrease in the barrier when both F and Li-excess are present (*b* vs. *d*).

By comparing configurations *f* vs. *d*, we can quantify that the increase of the KRA barrier when fluorine is added to the dumbbell in a 1-TM path is 140 meV. In contrast, when adding F to a 0-TM path, as in going from configuration *a* to *b*, the barrier increases by only 40 meV. Note that the purpose of this comparison is not to quantify the barriers exactly but to demonstrate that the increase of the migration barrier due to the presence of F is larger in the 1TM channel than in the 0TM channel. The origin of this variation of barrier increase with F can be elucidated by inspecting the actual migration paths in Figure S4. For a 0-TM path the migrating Li can "escape" from the F in the dumbbell by bowing the path more into the 0-TM tetrahedron, thereby lessening the negative effect of F on the barrier. This is not the case for a 1-TM path where the repulsion with the TM keeps the migrating Li close to the F in the dumbbell. This analysis shows that increase of barrier by F is not constant and may depend on the species present in the local environment of the migrating ion, as the negative effect of F is smaller when Li-excess is present.

NEB calculations are subject to the errors of DFT calculations (37)**.** Though the accuracy of DFT barriers has never been firmly established across a large set of structures and chemistries, based on our experience, we estimate that the calculated migration barriers have an error bar of ~0.1 eV (38)**.** In a recent study, it has been mentioned that the experimental error of activation barriers across different labs is about 128 meV for known conductors (39). However, given that we compare barriers in similar structures and chemistries, we expect our relative differences to be more accurate than 0.1eV.

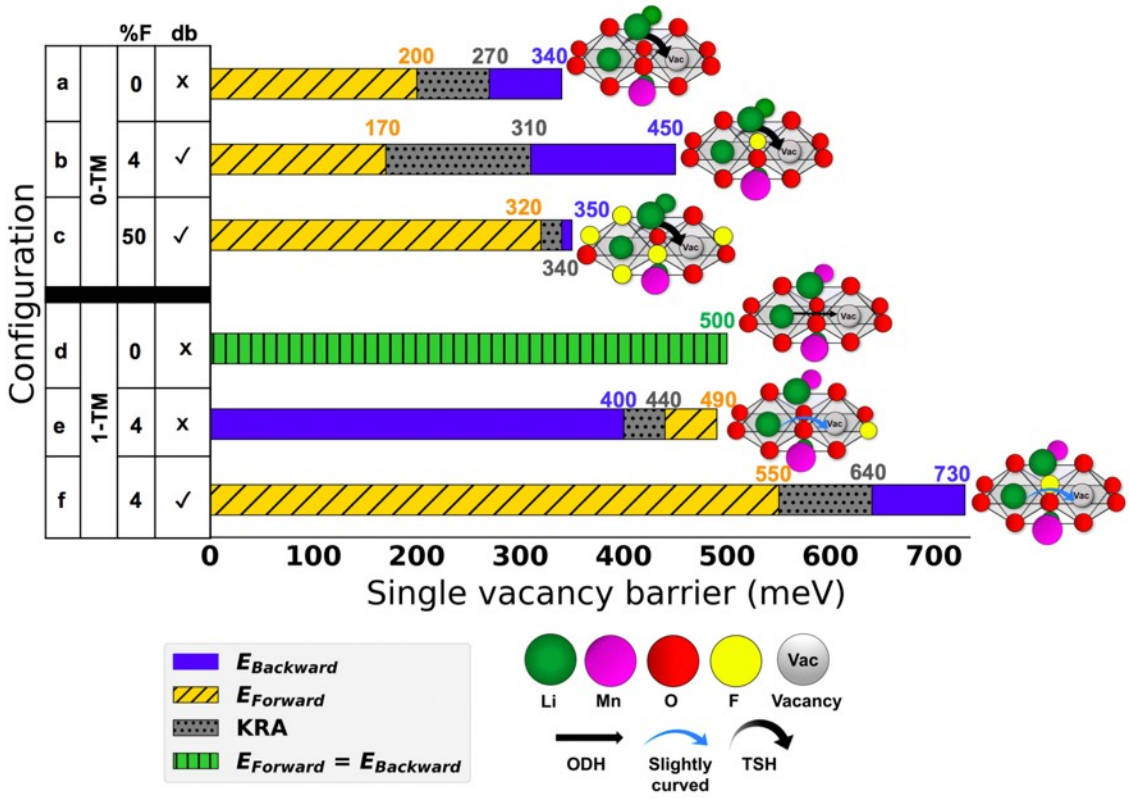

Figure 2: Horizonal bar chart showing the single vacancy diffusion barriers for various local configurations around a migrating Li. The black and blue arrows in each of the atomic configurations show schematically the Li migration trajectory. Li, Mn, O, F, and vacancy are shown as green, purple, red, yellow, and light gray spheres. The table attached to the *y* axis of the bar chart describes the local atomic configurations. The column labeled "%F" refers to F concentration, and the column labeled "db" refers to whether the F is in the anion dumbbell or not. The family of 0-TM bars correspond to the cases when Li-excess is present. Solid blue bars, striped yellow bars, and dotted gray bars, which are superimposed, show the backward energy, forward energy, and KRA barriers for each local environment. For symmetric local

environments, a single vertically striped green bar is used because the forward, backward, and KRA barriers are equal. See Figures S1, S4, and S6 for the corresponding MEPs.

C. Divacancy diffusion mechanism in presence of F and Li-excess

We also investigate the effect of F on a number of divacancy diffusion pathways. Figure 3 shows the barriers for divacancy Li migration in 4 different local environments following the same conventions as in Figure 2. Configuration *a* is the reference divacancy hop for the unfluorinated $LiMnO_2$ oxide with a KRA of 180 meV. Unlike the single vacancy hop in the pristine structure, the divacancy hop usually does not result in equivalent configurations before and after the hop, except in the most symmetric structures. Hence, the forward and backward diffusion barriers differ (also shown in the MEP in Figure S2), and the KRA is the most relevant quantity to extract (19) . Configurations *b* and *c* correspond to hops with F in different locations around the endpoint of the trajectory, while configuration *d* has F in the anion dumbbell and is shared among the polyhedra defining the initial, final, and intermediate sites. Most KRA barriers are in the range of 200 meV when no F is present in the dumbbell. With F in the dumbbell the KRA is significantly higher (configuration *d*), similar to what is observed for the single vacancy migration mechanism.

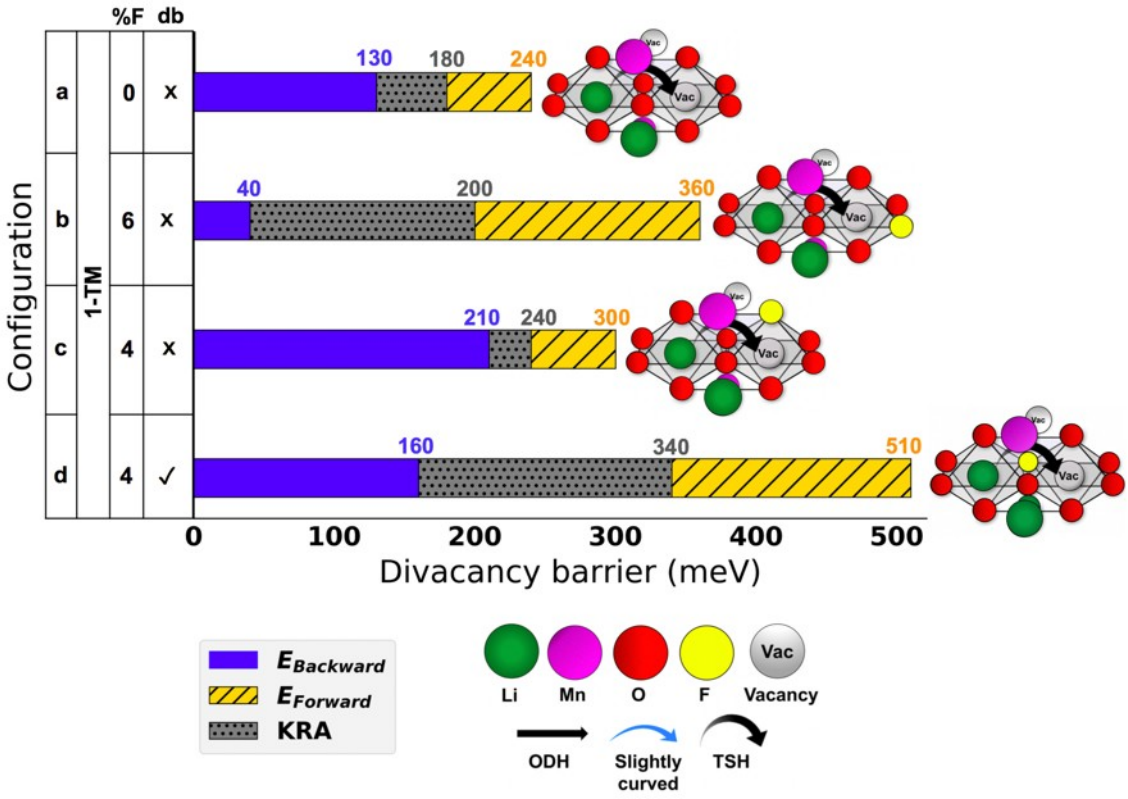

Figure 3: Horizonal bar chart showing the divacancy migration barriers for various local configurations around a migrating Li. The black arrows in each of the atomic configurations show schematically the Li trajectory obtained from NEB relaxation. Li, Mn, O, F, and vacancy are shown as green, purple, red, yellow, and light gray spheres. The table attached to the *y* axis of the bar chart describes the local atomic configurations. The column labeled "%F" refers to F concentration, and the column labeled "db" refers to whether the F is in anion dumbbell or not. Solid blue bars, striped yellow bars, and dotted gray bars show the backward, forward, and KRA barriers for each local environment. Figure S3 compares the MEP of the pristine structure (configuration *a*) with the 4% F structure (configuration *d)*.

D. F bonding preferences

Our previous results have focused on the barriers of Li migration in various local atomic configurations. When the initial and final sites are not equivalent, their Li site energy difference

contributes to the barrier negatively or positively depending on the direction of the jump. It has been previously reported that in cation-filled rocksalts F prefers coordination to Li rather than to TM due to the high energy of TM-F bonds (15,23), but it has not yet been investigated how F will interact in the presence of both Li and vacancies. To better understand the effect of F on Li site energies and Li transport, we additionally investigate the bonding preferences of F through both NEB results and the calculation of vacancy formation energies in varying configurations.

Figure 4 shows NEB calculations for Li diffusion via the single vacancy mechanism when a single F is substituted for an O on varying anion sites (labeled p1-p10) around the diffusing Li ion. Migration paths p1 and p6 have a F in the anion dumbbell and the highest KRA barriers. This is in line with our previous results showing that the substitution of an F in the anion dumbbell increases the barrier more than the substitution of F in other locations. Moving the Li atom from an initial state without F bonding to a F-bonded final state increases the energy as observed for migration in configurations p2-p5. In migration paths p7-p10, the Li escapes from the F-bonded higher energy initial site to the non-F bonded lower energy final site. These results indicate that fluorine prefers coordination by the vacancy rather than by Li in this system. Hence, jumps whereby Li moves towards a F will have a higher barrier than the reverse jumps. As shown in the horizontal bar chart in Figure 4 (right), the KRA of all positions of F are almost the same (~500 meV), except configurations with F in p1 and p6 which have about 100 meV higher KRA (~600 meV) than other positions.

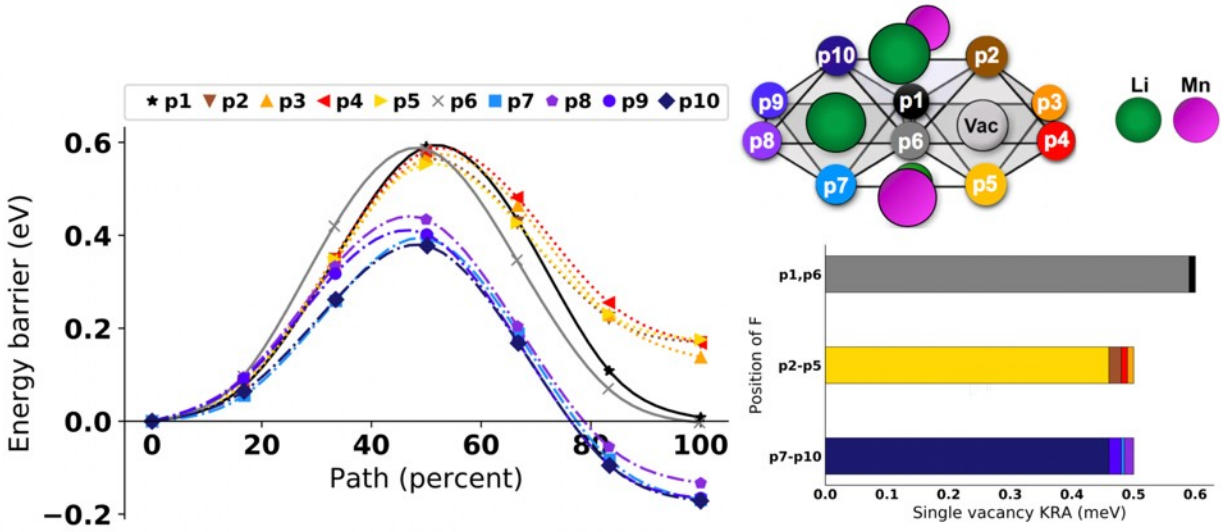

Figure 4: Li hopping in single vacancy mechanism (out-of-plane, ODH hop) with a single F in varying sites around the migrating Li. 1 F is substituted for O in different anion sites (p1 to p10 in the atomic configuration inset). The family of blueish lines correspond to paths where F is bonded to only the initial state of the diffusing atom, the family of yellowish/brown lines corresponds to the paths where F is bonded to only the final state, and the black/dark gray lines correspond to the paths where F is bonded to both the initial and final states. The green, purple, and red circles in the inset correspond to Li, Mn, and O, respectively. A horizontal bar chart corresponding to KRA of p1 to p10 are plotted to the right of the figure.

In order to confirm our findings on F bonding preferences, we also evaluate the voltage required to remove a Li (create a Li vacancy) at increasing distance from a F. Figure 5 demonstrates that it requires increasing voltage to remove a Li (create a vacancy) as the removed Li is at increasing distance from F, confirming that F stabilizes vacancies in its near neighbor shell.

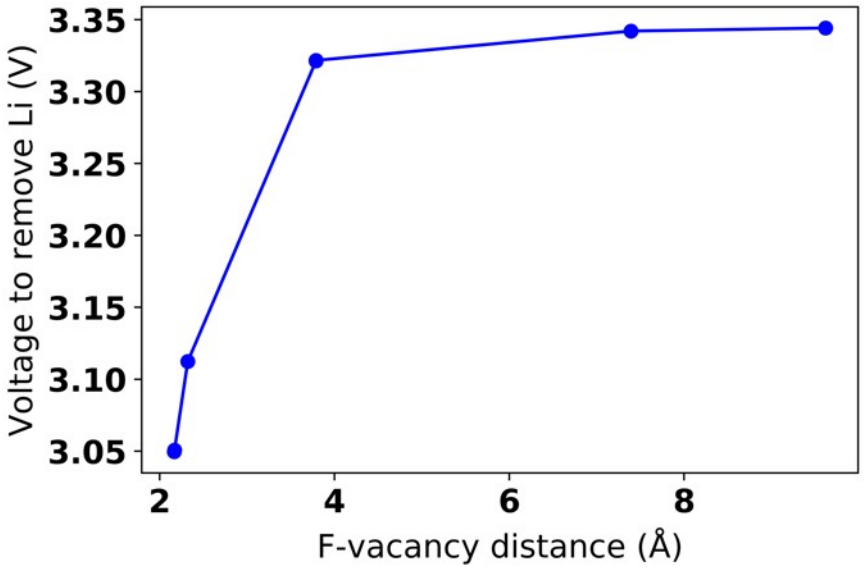

Figure 5: Voltage (V) required to create a Li-vacancy as a function of distance of the vacancy to the F anion in a ~2% fluorinated supercell of o-$LiMnO_2$ ($Li_{65}Mn_{63}O_{126}F_2$).

DISCUSSION

We investigated the effect of fluorine substitution on Li migration and Li site energies in o-$LiMnO_2$ as a prototypical Mn-based cathode material that contains different local environments representative of those that can be found in disordered structures. Figure 6 compares the energy barriers in our model system with computed data available in literature for well known intercalation materials, including layered ($LiMO_2$ for M=Ti, V, Cr, Ni (40), Co (41), $Li(Ni_{0.5}Mn_{0.5})O_2$ (42), and $Li(Ni_xMn_yCo_z)O_2$ (NMC) (43)), spinel ($Li_{1+x}Mn_{2-x}O_4$ (x=0, 0.125) (44), Li_xTiS_2 (18), and $LiNi_{0.5}Mn_{1.5}O_4$ (45)), and olivine ($LiM(=Mn,Fe,Co,Ni)PO_4$ (46) and $Li_{1+x}Fe_{1-x}PO_4$, which contains Li-excess on the Fe sites of $LiFePO_4$ (47)) systems. As Li migration barriers depend on various environmental factors, we indicate with polygons where variations in the

barrier originate and with a double star adjacent to the structure name which materials are disordered, as the local environments vary greatly in these systems. We also depict the type of hop using differently colored bars.

According to Figure 6, the range of migration barriers for TSH mechanism in our model system (~240 meV to ~500 meV) overlaps with TSH barriers for the $LiCoO_2$ (~200 meV to ~600 meV) and NCM (~357 meV to ~545 meV) cathode materials. In our model system, the ODH mechanism (~490 meV to ~730 meV) typically results in lower migration barriers than in $LiCoO_2$ (~700 meV to ~950 meV) and NMC (~750 meV to ~900 meV) which can be explained by differences in structural geometry (orthorhombic vs. layered) and chemistry of these materials.

Furthermore, the overall range of barriers calculated in our model system (~240 meV to ~700 meV) is very similar to range of barriers in stochimetric and Li-excess spinel Mn oxides (~240 meV to ~810 meV). It is important to note that the migrating Li-ions always take the path with lowest activation barrier in order to percolate throughout the structure. However, since there is not much information available about how the disorder in these specific systems (such as Mn-based Li-excess spinel) affects the percolation path, we compare the overall range and distribution of barriers. The similar overall ranges between the model system and Li-excess spinel oxides thus further supports our finding that effect of F incorporation on Li diffusion is not expected to be significant and that the migration barriers calculated in this work remain in a reasonable range.

One of the main factors that result in having high power density is to have high Li-ion diffusivity (42,43). The diffusivity of successful commercialized cathodes such as $LiCoO_2$ is around 10^{-12} to 10^{-11} cm^2/s (48). If we assume a hop distance of 3 Å for Li-ions and a vibrational prefactor of

10^{11}-10^{12} s^{-1} in a simple random walk model for diffusivity, the diffusion coefficient needed to (de)lithiate a 1 micron particle in 1 hr (estimating diffusion distance as the square root of the diffusivity x time) is associated with an upper range of acceptable activation barriers of $\approx$ 400-450 meV. Most of the migration barriers for the TSH hop in our model system are below 450 meV, including single vacancy barriers in the presence of Li-excess (Figure 2, environments *a*, *b* and *c*) and all divacancy mechanisms except one with F in the anion dumbbell (Figure 3, environments *a*, *b*, *c*). These low migration barriers indicate that Li will likely be able to find a percolation path through the lower-energy hops as long as TSH mechanism becomes available.

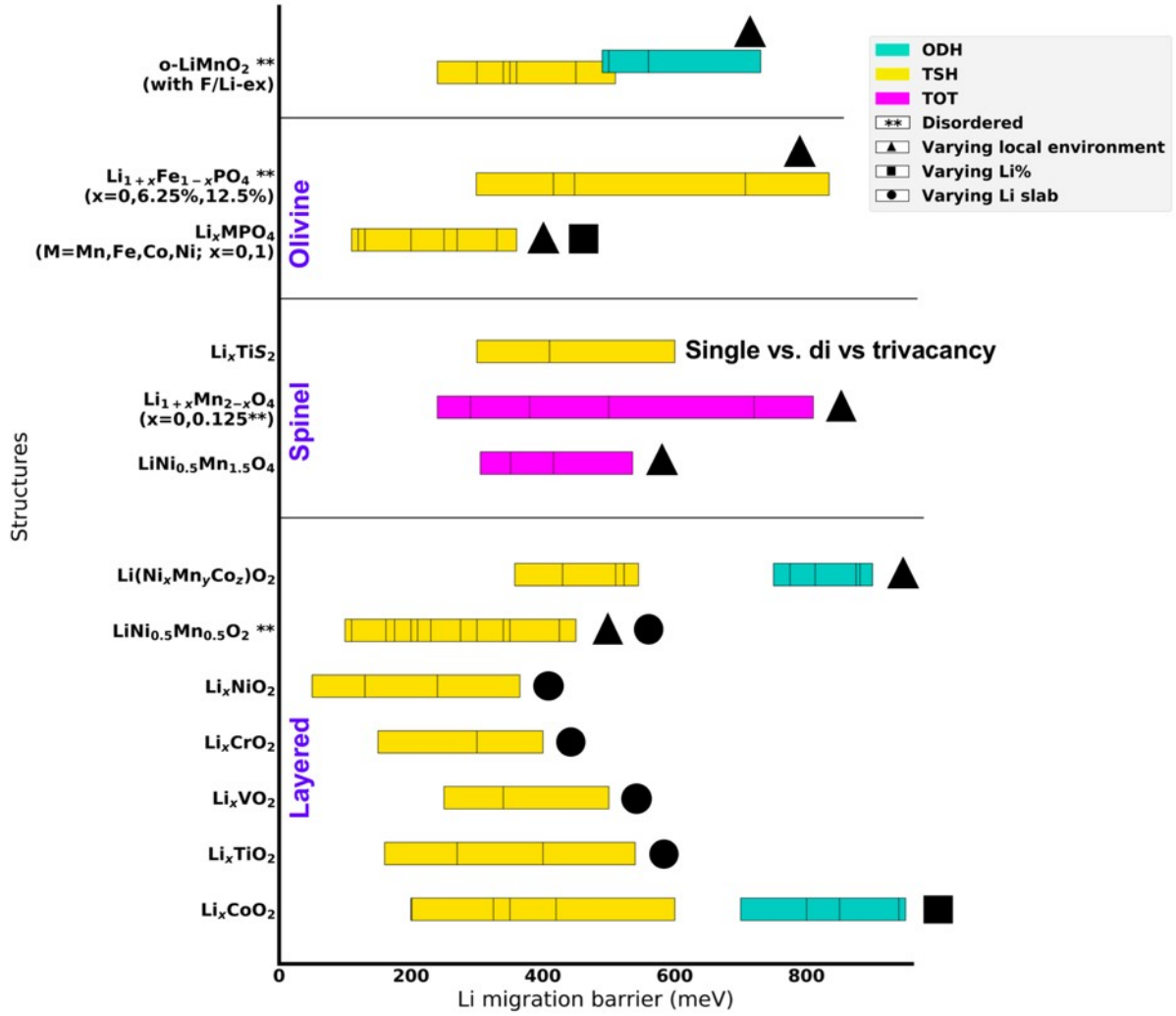

Figure 6: Comparison between activation barriers of the model system (o-$LiMnO_2$ with and without F/Li-excess) via both ODH and TSH mechanisms with available migration barriers for ODH and TSH mechanisms for various delithiated states of different layered, spinel, and olivine systems in literature. The barriers for ODH, TSH, and tetrahedral to octahedral to tetrahedral (TOT) paths are shown as turquoise, yellow, and magenta bars respectively. Double stars (**) next to the name of the structure indicate a disordered structure. In the case of $Li_{1+x}Mn_{2-x}O_4$, only the Li-excess phase (x=0.125) is disordered. The polygons near the bars (triangle, square, and

circle) specify where variations in the barriers come from (varying local environment, Li concentration, and Li slab space, respectively).

Our findings show that F substitution modifies the migration barrier, path, and site energy. Together with the Li-excess that can be co-introduced with F substitution these form an interrelated set of effects which we have tried to deconvolute in this work by evaluating the barrier when the local environment is systematically modified. We find that, when all else remains identical in the environment, the substitution of F for O tends to raise the Li migration barriers somewhat, with the strongest increase occuring when F is substituted in the anion edge (dumbell) that is shared between the anion octahedra coordinating the final and initial Li site. The most significant increase of KRA is found for single vacancy migration with 1-TM tetrahedral configurations present around the path (Figure 2, environment *f)*, as the presence of TM on both the tetrahedral channels as well as the F in the dumbell create a highly constrained environment for Li to migrate through. But the high activation energy for this mechanism makes it all but irrelevant even in unfluorinated compounds. The effect of F in the dumbell on the single vacancy barrier is significantly mitigated when a 0-TM tetrahedron is present around the migration path as it allows the path to bow away from the F-containing edge (Figure 2, environement *b*). In the latter environment, F in the dumbell only increases the KRA by 40 meV, as compared to an increase of 140 meV when no 0-TM environment is present (Figure 2, environments *f* and *d*). Hence, Li-excess or appropriate short range order (SRO) (49), which create 0-TM environment is an important aspect of mitigating the effect of F on the migration barrier.

We confirm that the barriers for the divacancy mechanism are considerably lower than for the single vacancy migration, consistent with the literature (17), but also increase the most when F is present in the anion dumbell shared between the initial and final state octahedron. When F is present in sites that only coordinate the initial or final cation site, the path becomes asymmetric with only a small increase in the KRA. While we only showed 1-TM divacancy hops in Figure 3, we also investigated the divacancy mechanism with a 0-TM channel with presence of F in the anion dumbbell (Figure S8) and find that the octahedral sites are unstable and relax into the tetrahedral site. Euchner et al. has reported a similar obseration in V and Ti disordered rocksalt materials in the presence of only Li-excess and two or more vacancies (50). Previously, in a study that investigated the 0-TM diffusion barrier in special quasi-random structures (SQS) of fluorinated $LiTiO_2$, it was found that the combination of Li-excess and fluorination also resulted in a stronger stabilization of the tetrahedral site compared to Li-excess alone (16). The stabilization of the tetrahedral site may be assisted by the two octahedral vacancies near F that it creates. Because the tetrahedral site is only stabilized by $\approx$ 150meV over the octahedral sites, this site shift is not expected to impede Li migration.

The effect of F^- on the transition path and site energy can be rationalized from its different electron configuration compared to O^{2-}. Its lower negative charge results in less attraction to the Li^+ cation to compensate for the Pauli (steric) repulsion between the ions. This net repulsion is responsible for the single vacancy migration path bowing out but not bending completely into the tetrahedral site when F is in the anion dumbbell (Figure 2). It also explains the net attraction of F to a vacancy which creates asymmetry in the forward and backward path of jumps. In addition,

the lower polarizability of F^- compared to O^{2-} limits its ability to screen Li^+'s repulsion from other cations resulting in a higher site energy and generally higher barriers.

While the presence of F has a small negative effect on Li migration, Li-excess is found to drastically decrease the migration barrier by transforming 1-TM channels into 0-TM channels, which reduces the diffusion barriers for both single vacancy and divacancy diffusion mechanisms. Comparing configurations *d* vs. *a* and *f* vs. *b* in Figure 2 shows that the presence of Li-excess decreases the barrier by more than 200 meV, which is in line with previous results showing that 1-TM channels are 200-300 meV higher in energy barrier than 0-TM channels (20). While it is generally assumed that Li migration occurs through divacancies we find that in a Li-excess environment (0-TM channels) even the single vacancy mechanism may be active, as its KRA values are of the order of 300 meV, which is low enough for them to actively contribute to Li transport in the cathode material. This may be particularly important at the end of discharge where vacancies are scarce which may make the divacancy diffusion mechanism inaccessible. To make an overall assessment of the effect of fluorination on Li transport one needs to combine both its effect on the percolation as investigated in other work (16) and its effect on local migration barriers. Previous work showed that for oxides with good 0-TM percolation, at fixed Li-excess, small amounts of F lower the percolation of 0-TM channels, whereas amounts above 15% improve percolation. However, for oxides with poor 0-TM percolation, fluorination should always be beneficial (16). Because we find that Li migration through 0-TM environments is minimally affected by F substitution it is possible to conclude that no large changes in bulk Li diffusion rates should be expected when DRX materials are fluorinated.

Our results indicate an interesting possible trade-off between rate and stable capacity in fluorinated materials. If F substitution in the material is used to increase the Li-excess content,

then the combined effect is likely to be highly favorable for Li transport as the increase in Li-excess will outweigh the small effect of F on the barriers. In contrast, when fluorination is used to increase the TM redox capacity, as originally intended (23,51), its effects on rate will depend strongly on the amount of Li-excess already present.

Finally, our results also indicate some potential complications that can arise with F incorporation. The attraction of F to the single Li vacancy may trap vacancies at dilute concentrations, which indicates that a small amount of F might impede Li transport at early stages of charge. If the F content is high enough for F ions to share vacancies, then this effect is likely to be diminished. A quantitative evaluation of this effect would require more extensive kinetic studies similar to those performed for Li_xCoO_2 (19,41), but the complexity of this system with its disorder over multiple cation and anion components will make this challenging. SRO has been observed in disordered rock salts and has been argued to affect the amount of percolating Li (16,52). However, to our knowledge there is no strong evidence of ordering or inhomogeneity on the nanoscale.

Somewhat surprisingly, we find in our work barriers of some 1-TM channels that are low enough to participate in Li diffusion. We believe that this is a result of our choice of model system. While o-$LiMnO_2$ has multiple distinct environments, making it a useful system to study the environment dependence of the barrier, the height of the tetrahedral site in o-$LiMnO_2$ is approximately 2.53 Å while the typical tetrahedron height in a disordered rocksalt structure is shorter and typically below 2.40 Å (20). This height of the tetrahedron has been show to influence in particular the 1-TM barrier (but less so the 0-TM barrier) (20). Hence, 1-TM channels are probably somewhat disproportionally favored over 0-TM channels in our calculations.

Our calculations focused on the Mn systems, but recent work has found that there may be significant differences in the effect of F arising from the TM metal chemistry (50). While the reason for this chemistry dependence is not clear, it is possible that chemistry modifies the geometry of the path. As our results indicate, the impact of F on the barrier is less significant when the migrating Li can evade F by bowing into the tetrahedral site, which would be much easier in larger tetrahedral sites. In that context, Euchner et al (50) point at the potential reduction of the TM at the gate site as an important variable to affect the barrier, Such an electrochemical process would lead to F having chemistry dependent effects on the barrier.
In this work we have only looked at the Li diffusion in the early stages of charge where there is no oxygen oxidation. At the end of charge, due to oxygen oxidation, there might be some effect on Li mobility although that effect would likely be less important in F-substituted materials.

Conclusion

In this work, we used first principles calculations to investigate the impact of fluorine substitution on the Li migration energy in orthorhombic $LiMnO_2$ as a model for Mn-based DRX systems. While our results show a small increase in most kinetically resolved barriers in the proximity of F, they are mostly negated in the presence of Li-excess. Hence, one can expect that systems that are 0-TM percolating will have reasonable Li transport, with or without F in the composition.

Conflicts of interest

There are no conflicts to declare.

ACKNOWLEDGEMENTS

This work was supported by the Assistant Secretary for Energy Efficiency and Renewable Energy, Vehicle Technologies Office, under the Applied Battery Materials Program, of the U.S.

Department of Energy under Contract No. DE-AC02-05CH11231. The computational analysis was performed using computational resources sponsored by the Department of Energy's Office of Energy Efficiency and Renewable Energy and located at the National Renewable Energy Laboratory as well as computational resources provided by Extreme Science and Engineering Discovery Environment (XSEDE), supported by National Science Foundation grant number ACI1053575, and the National Energy Research Scientific Computing Center (NERSC), a DOE Office of Science User Facility supported by the Office of Science and the U.S. Department of Energy under Contract No. DE-AC02-05CH11231. Part of P. X.'s work was performed under the auspices of the U.S. Department of Energy by Lawrence Livermore National Laboratory under Contract Number DE-AC52-07NA27344. ZJ and TC acknowledge financial support from the NSF Graduate Research Fellowship Program (GRFP) under Contract No. DGE 1752814 and Contract No. DGE 1106400. Any opinions, findings, and conclusions or recommendations expressed in this material are those of the author(s) and do not necessarily reflect the views of the National Science Foundation.

REFERENCES

1. Chen R, Ren S, Yavuz M, Guda AA, Shapovalov V, Witter R, et al. Li+ intercalation in isostructural Li2VO3 and Li2VO2F with O2− and mixed O2−/F− anions. Phys Chem Chem Phys. 2015 Jun 24;17(26):17288–95.

2. Cambaz MA, Vinayan BP, Geßwein H, Schiele A, Sarapulova A, Diemant T, et al. Oxygen Activity in Li-Rich Disordered Rock-Salt Oxide and the Influence of LiNbO3 Surface Modification on the Electrochemical Performance. Chem Mater. 2019;31(12):4330–4340.

3. Clément RJ, Lun Z, Ceder G. Cation-disordered rocksalt transition metal oxides and oxyfluorides for high energy lithium-ion cathodes. Energy Environ Sci. 2020 Feb 19;13(2):345–73.

4. Lun Z, Ouyang B, Kitchaev DA, Clément RJ, Papp JK, Balasubramanian M, et al. Improved Cycling Performance of Li-Excess Cation-Disordered Cathode Materials upon Fluorine Substitution. Adv Energy Mater. 2019;9(2):1802959.

5. Redel K, Kulka A, Plewa A, Molenda J. High-performance Li-rich layered transition metal oxide cathode materials for Li-ion batteries. J Electrochem Soc. 2019;166(3):A5333–A5342.

6. Lee J, Kitchaev DA, Kwon D-H, Lee C-W, Papp JK, Liu Y-S, et al. Reversible Mn 2+/Mn 4+ double redox in lithium-excess cathode materials. Nature. 2018;556(7700):185–190.

7. Lun Z, Ouyang B, Cai Z, Clément RJ, Kwon D-H, Huang J, et al. Design Principles for High-Capacity Mn-Based Cation-Disordered Rocksalt Cathodes. Chem. 2020;6(1):153–168.

8. Olivetti EA, Ceder G, Gaustad GG, Fu X. Lithium-Ion Battery Supply Chain Considerations: Analysis of Potential Bottlenecks in Critical Metals. Joule. 2017 Oct 11;1(2):229–43.

9. House RA, Maitra U, Jin L, Lozano JG, Somerville JW, Rees NH, et al. What triggers oxygen loss in oxygen redox cathode materials? Chem Mater. 2019;31(9):3293–3300.

10. Seo D-H, Lee J, Urban A, Malik R, Kang S, Ceder G. The structural and chemical origin of the oxygen redox activity in layered and cation-disordered Li-excess cathode materials. Nat Chem. 2016 Jul;8(7):692–7.

11. Chen D, Kan WH, Chen G. Understanding Performance Degradation in Cation-Disordered Rock-Salt Oxide Cathodes. Adv Energy Mater. 2019;9(31):1901255.

12. Kan WH, Chen D, Papp JK, Shukla AK, Huq A, Brown CM, et al. Unravelling solid-state redox chemistry in Li1. 3Nb0. 3Mn0. 4O2 single-crystal cathode material. Chem Mater. 2018;30(5):1655–1666.

13. Koga H, Croguennec L, Ménétrier M, Douhil K, Belin S, Bourgeois L, et al. Reversible oxygen participation to the redox processes revealed for Li1. 20Mn0. 54Co0. 13Ni0. 13O2. J Electrochem Soc. 2013;160(6):A786–A792.

14. Armstrong AR, Holzapfel M, Novák P, Johnson CS, Kang S-H, Thackeray MM, et al. Demonstrating oxygen loss and associated structural reorganization in the lithium battery cathode Li [Ni0. 2Li0. 2Mn0. 6] O2. J Am Chem Soc. 2006;128(26):8694–8698.

15. Kitchaev DA, Lun Z, Richards WD, Ji H, Clément RJ, Balasubramanian M, et al. Design principles for high transition metal capacity in disordered rocksalt Li-ion cathodes. Energy Environ Sci. 2018;11(8):2159–2171.

16. Ouyang B, Artrith N, Lun Z, Jadidi Z, Kitchaev DA, Ji H, et al. Effect of Fluorination on Lithium Transport and Short-Range Order in Disordered-Rocksalt-Type Lithium-Ion Battery Cathodes. Adv Energy Mater. 2020;1903240.

17. Van der Ven A, Ceder G. Lithium diffusion mechanisms in layered intercalation compounds. J Power Sources. 2001 Jul 1;97–98:529–31.

18. Van der Ven A, Bhattacharya J, Belak AA. Understanding Li diffusion in Li-intercalation compounds. Acc Chem Res. 2013;46(5):1216–1225.

19. Van der Ven A, Ceder G, Asta M, Tepesch PD. First-principles theory of ionic diffusion with nondilute carriers. Phys Rev B. 2001;64(18):184307.

20. Lee J, Urban A, Li X, Su D, Hautier G, Ceder G. Unlocking the potential of cation-disordered oxides for rechargeable lithium batteries. science. 2014;343(6170):519–522.

21. Ceder G, Mishra SK. The Stability of Orthorhombic and Monoclinic-Layered LiMnO2. Electrochem Solid State Lett. 1999;2(11):550.

22. Jang Y-I, Chou FC, Huang B, Sadoway DR, Chiang Y-M. Magnetic characterization of orthorhombic LiMnO2 and electrochemically transformed spinel LixMnO2 (x< 1). J Phys Chem Solids. 2003;64(12):2525–2533.

23. Richards WD, Dacek ST, Kitchaev DA, Ceder G. Fluorination of Lithium-Excess Transition Metal Oxide Cathode Materials. Adv Energy Mater. 2018;8(5):1701533.

24. Hohenberg P, Kohn W. Inhomogeneous electron gas. Phys Rev. 1964;136(3B):B864.

25. Kohn W, Sham LJ. Self-consistent equations including exchange and correlation effects. Phys Rev. 1965;140(4A):A1133.

26. Perdew JP, Burke K, Ernzerhof M. Generalized gradient approximation made simple. Phys Rev Lett. 1996;77(18):3865.

27. Blöchl PE. Projector augmented-wave method. Phys Rev B. 1994;50(24):17953.

28. Kresse G, Joubert D. From ultrasoft pseudopotentials to the projector augmented-wave method. Phys Rev B. 1999;59(3):1758.

29. Kresse G, Furthmüller J. Efficiency of ab-initio total energy calculations for metals and semiconductors using a plane-wave basis set. Comput Mater Sci. 1996;6(1):15–50.

30. Kresse G, Furthmüller J. Efficient iterative schemes for ab initio total-energy calculations using a plane-wave basis set. Phys Rev B. 1996;54(16):11169.

31. Dudarev SL, Botton GA, Savrasov SY, Humphreys CJ, Sutton AP. Electron-energy-loss spectra and the structural stability of nickel oxide: An LSDA+ U study. Phys Rev B. 1998;57(3):1505.

32. Jain A, Ong SP, Hautier G, Chen W, Richards WD, Dacek S, et al. Commentary: The Materials Project: A materials genome approach to accelerating materials innovation. Apl Mater. 2013;1(1):011002.

33. Henkelman G, Jónsson H. Improved tangent estimate in the nudged elastic band method for finding minimum energy paths and saddle points. J Chem Phys. 2000;113(22):9978–9985.

34. Urban A, Seo D-H, Ceder G. Computational understanding of Li-ion batteries. Npj Comput Mater. 2016;2(1):1–13.

35. Asari Y, Suwa Y, Hamada T. Formation and diffusion of vacancy-polaron complex in olivine-type LiMnPO 4 and LiFePO 4. Phys Rev B. 2011;84(13):134113.

36. Kong F, Longo RC, Park M-S, Yoon J, Yeon D-H, Park J-H, et al. Ab initio study of doping effects on LiMnO 2 and Li 2 MnO 3 cathode materials for Li-ion batteries. J Mater Chem A. 2015;3(16):8489–8500.

37. Zarkevich NA, Johnson DD. Nudged-elastic band method with two climbing images: Finding transition states in complex energy landscapes. J Chem Phys. 2015;142(2):024106.

38. Henkelman G. Methods for calculating rates of transitions with application to catalysis and crystal growth [PhD Thesis]. 2001.

39. Ohno S, Bernges T, Buchheim J, Duchardt M, Hatz A-K, Kraft MA, et al. How certain are the reported ionic conductivities of thiophosphate-based solid electrolytes? An interlaboratory study. ACS Energy Lett. 2020;5(3):910–915.

40. Kang K, Ceder G. Factors that affect Li mobility in layered lithium transition metal oxides. Phys Rev B. 2006 Sep 26;74(9):094105.

41. Van der Ven A, Ceder G. Lithium diffusion in layered Li x CoO2. Electrochem Solid-State Lett. 2000;3(7):301–304.

42. Kang K. Electrodes with High Power and High Capacity for Rechargeable Lithium Batteries. Science. 2006 Feb 17;311(5763):977–80.

43. Wei Y, Zheng J, Cui S, Song X, Su Y, Deng W, et al. Kinetics Tuning of Li-Ion Diffusion in Layered Li(Ni $_x$ Mn $_y$ Co $_z$)O $_2$. J Am Chem Soc. 2015 Jul 8;137(26):8364–7.

44. Xiao W, Xin C, Li S, Jie J, Gu Y, Zheng J, et al. Insight into fast Li diffusion in Li-excess spinel lithium manganese oxide. J Mater Chem A. 2018;6(21):9893–9898.

45. Ma X, Kang B, Ceder G. High rate micron-sized ordered LiNi0. 5Mn1. 5O4. J Electrochem Soc. 2010;157(8):A925–A931.

46. Morgan D, Van der Ven A, Ceder G. Li conductivity in Li x MPO 4 (M= Mn, Fe, Co, Ni) olivine materials. Electrochem Solid State Lett. 2003;7(2):A30.

47. Zeng H, Gu Y, Teng G, Liu Y, Zheng J, Pan F. Ab initio identification of the Li-rich phase in LiFePO 4. Phys Chem Chem Phys. 2018;20(25):17497–17503.

48. Xia H, Meng SY, Lu L, Ceder G. Electrochemical Behavior and Li Diffusion Study of $LiCoO_2$ Thin Film Electrodes Prepared by PLD. 2007;

49. Ji H, Wu J, Cai Z, Liu J, Kwon D-H, Kim H, et al. Ultrahigh power and energy density in partially ordered lithium-ion cathode materials. Nat Energy. 2020 Mar;5(3):213–21.

50. Euchner H, Chang JH, Groß A. On stability and kinetics of Li-rich transition metal oxides and oxyfluorides. J Mater Chem A. 2020 Apr 28;8(16):7956–67.

51. Lee J, Papp JK, Clément RJ, Sallis S, Kwon D-H, Shi T, et al. Mitigating oxygen loss to improve the cycling performance of high capacity cation-disordered cathode materials. Nat Commun. 2017;8(1):1–10.

52. Ji H, Urban A, Kitchaev DA, Kwon D-H, Artrith N, Ophus C, et al. Hidden structural and chemical order controls lithium transport in cation-disordered oxides for rechargeable batteries. Nat Commun. 2019;10(1):1–9.

ADDITIONAL INFORMATION

Supplementary information

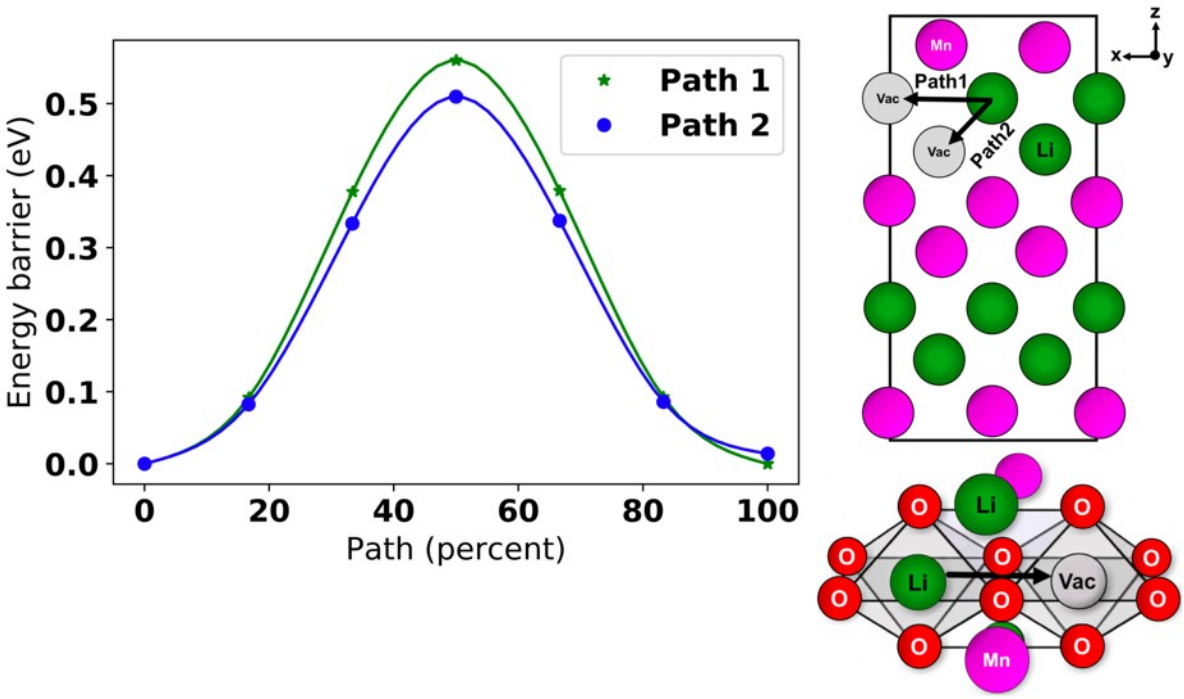

Figure S1: (left) Energy (eV) along the two possible paths (%) for a single vacancy mechanism in o-$LiMnO_2$. The in-plane hop (path 1) is shown in green with stars, and the out-of-plane hop (path 2) is shown in blue with filled circles. (bottom right) Magnified depiction showing the nearest neighbor cations along both paths. (top right) Atomic configuration demonstrating the Li hops, which occur along the trajectory shown by the black arrow along the (010) plane.

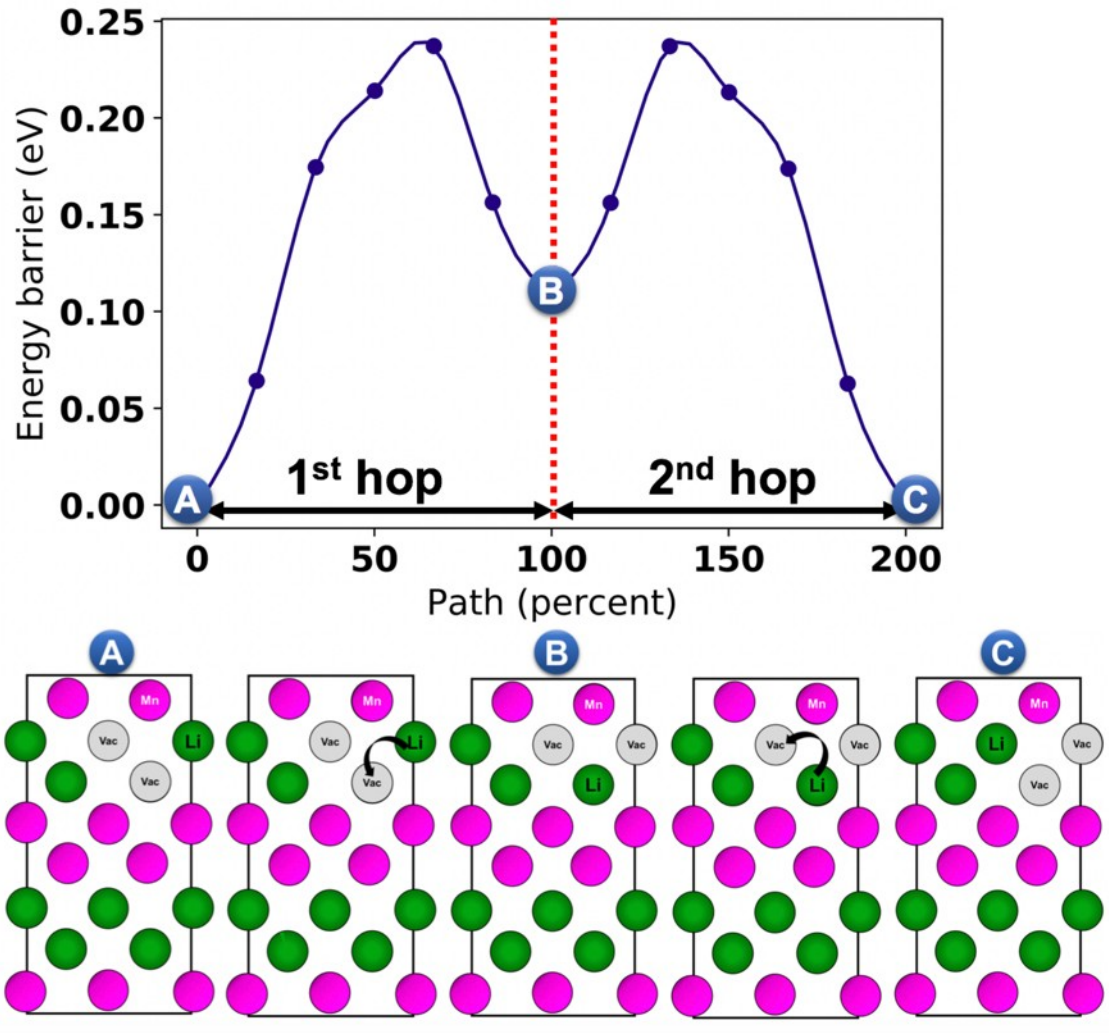

Figure S2: (top) Energy (eV) along Li migration path (%) consisting of two separate hops that constitute a full percolating path using the divacancy migration mechanism in o-$LiMnO_2$. (bottom) Atomic configurations of the hops before, during, and after the hops. Green, purple, and gray circles represent Li, Mn, and vacancies. O atoms are not shown for clarity. Position A in both top and bottom figures correspond to the case when two vacancies are not in the same plane but share an edge, while position B corresponds to the case when the vacancies are in the same plane. Position C is symmetrically equivalent to position A.

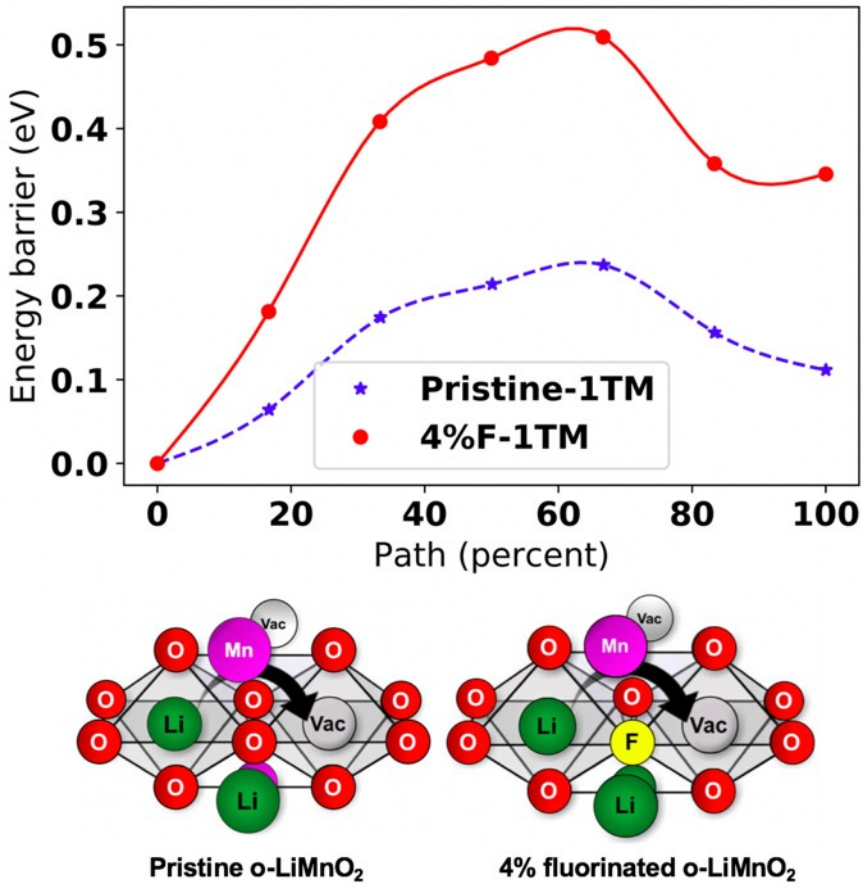

Figure S3: Energy (eV) along Li migration path (%) for 1-TM divacancy Li migration mechanism in pristine (dotted blue line) and 4% fluorinated o-$LiMnO_2$ (solid red line marked with filled circle). Atomic configurations are shown below the graph. Green, purple, red, yellow, and light gray show Li, Mn, O, F, and vacancy respectively.

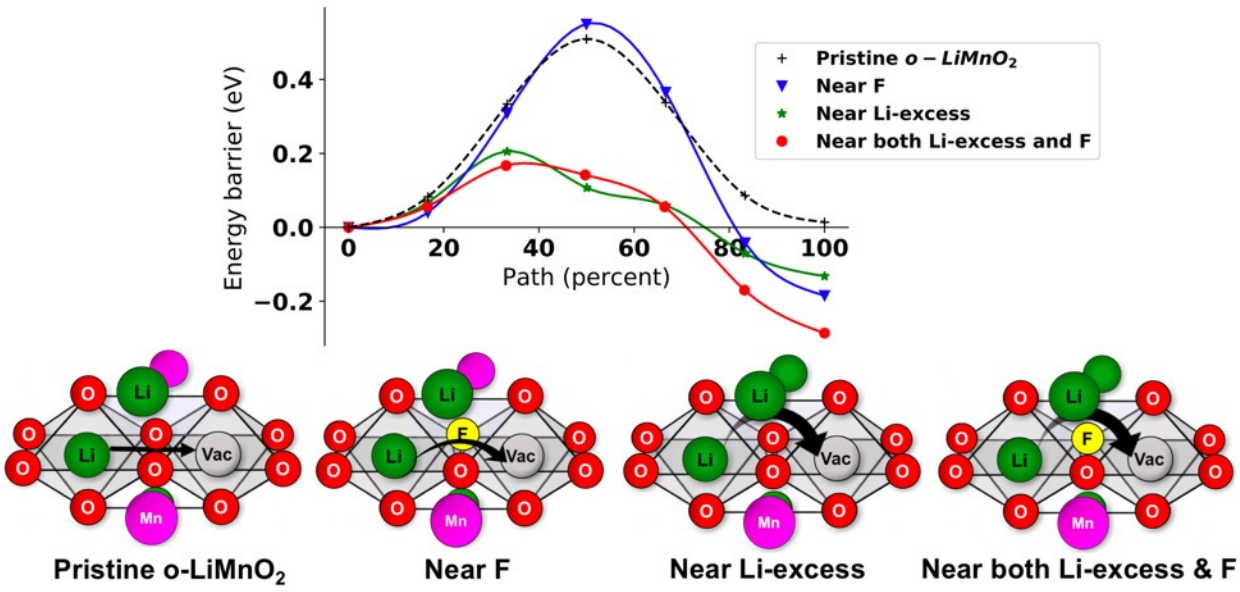

Figure S4: Energy (eV) along Li migration path (%) for single vacancy migration mechanism for cases when the migrating ion is in pristine o-$LiMnO_2$ (black dashed line, marked with plus sign), near F (solid blue curve, marked with triangle), near Li-excess (solid green curve, marked with star), and near both F and Li-excess (solid red color, marked with filled circle) from one octahedral site to another octahedral site. Atomic configurations are shown below the graph. Green, purple, red, yellow, and light gray show Li, Mn, O, F, and vacancy respectively. The black arrows on the atomic configurations correspond to the migration trajectory of the Li ion. Note that the o-$LiMnO_2$ has corrugated Li and Mn layers. Therefore, the initial and final sites of the migrating Li ion have different nearest neighbor cation environments in all cases except the pristine structure.

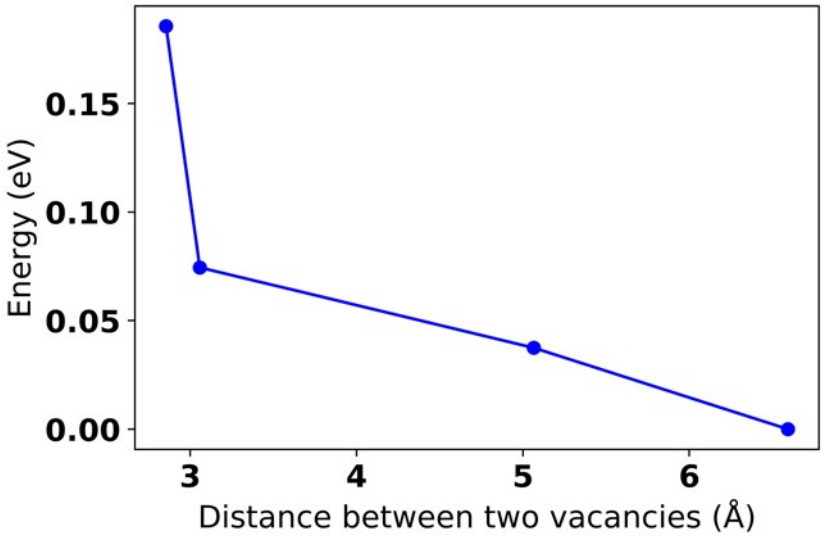

Figure S5: Energy (eV) of two vacancies separated at different distances. All the energies on the *y* axis are adjusted relative to the energy of the lowest energy configuration which here corresponds to a separation between two vacancies of 6.6 Å.

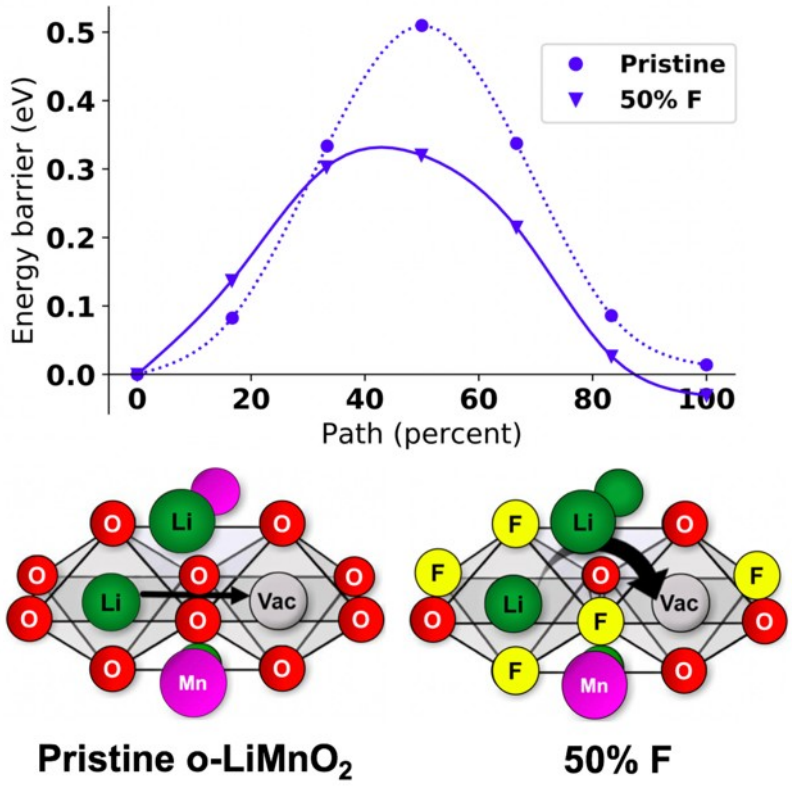

Figure S6: Energy (eV) along Li migration path (%) for 1-TM, out-of-plane hop (solid blue line) single vacancy Li migration mechanism in 50% fluorinated o-$LiMnO_2$. The MEP of the single vacancy migration mechanism for the pristine structure (dotted blue line) is replotted for the purpose of comparison. Atomic configurations are shown below the graph. Green, purple, red, yellow, and light gray show Li, Mn, O, F, and vacancy respectively.

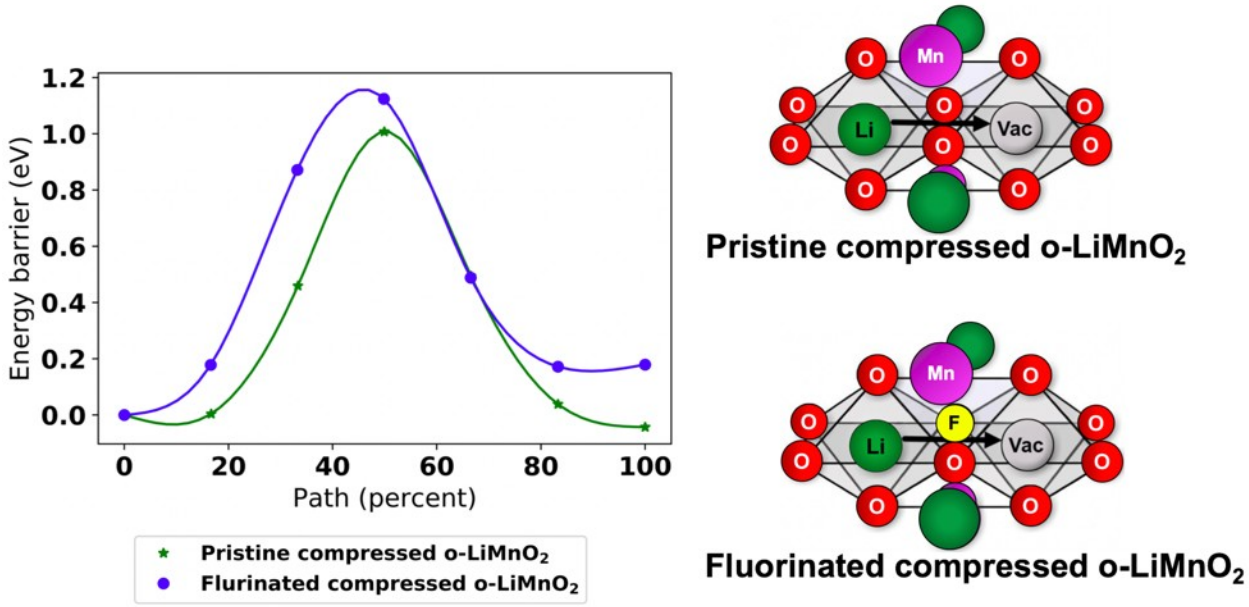

Figure S7: Energy (eV) along Li migration path (%) for 1-TM single vacancy Li migration mechanism in pristine and 3% fluorinated o-$LiMnO_2$ under compression. Atomic configurations are shown on the right. Green, purple, red, yellow, and light gray show Li, Mn, O, F, and vacancy respectively.

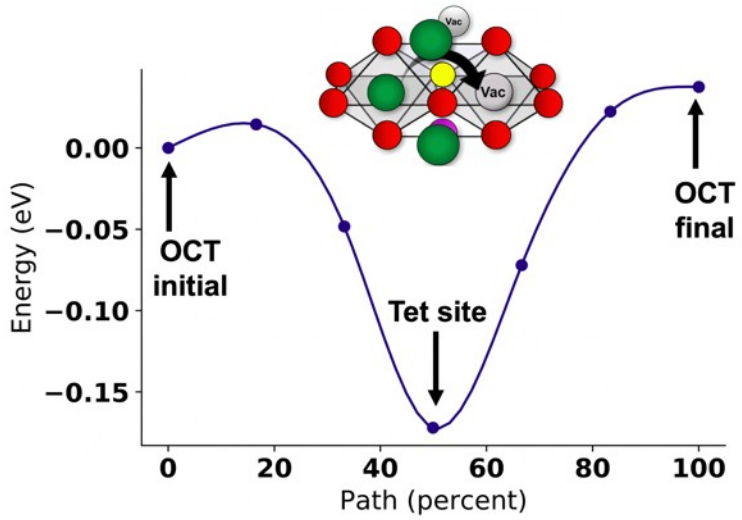

Figure S8: Energy landscapes along the migration path for 0-TM divacancy diffusion in a slightly fluorinated (4% F) o-$LiMnO_2$ structure. Also shown as an inset is the local atomic configurations with the Li trajectory shown by the black arrow in the atomic configurations, with black labels indicating the octahedral initial and final sites and tetrahedral intermediate sites. Li, Mn, O, F, and vacancy are depicted as green, purple, red, yellow, and light grey spheres.